Constrained asymptotic crack-tip fields of a Mooney–Rivlin sheet in plane stress: a symplectic analysis

Teng Zhang[a,b]

[a]Department of Mechanical and Aerospace Engineering, Syracuse University, Syracuse, NY 13244, USA

[b]BioInspired Syracuse, Syracuse University, Syracuse, NY 13244, USA

E-mail: tzhang48@syr.edu

Abstract

Analytical crack-tip fields for soft sheets are known mainly for generalized neo-Hookean materials. We formulate the crack-tip problem in a radial symplectic (Hamiltonian) framework, using $\xi = \ln r$ as the evolution coordinate. The deformation on a material circle and its weighted radial traction form the canonical pair, and the constraint reaction enters through the traction. Within this framework, dominant balance for an incompressible plane-stress Mooney–Rivlin sheet shows that the I_2 contribution becomes a kinematic constraint near the tip. The constraint drives the local state toward uniaxial tension. The leading stretch magnitudes are independent of angle, and the opening is $y_2 \sim Pr^{1/2}\sin(\theta/2)$. The compensated areal Jacobian $Jr^{1/4}$ approaches an angle-independent plateau. The same field gives $G = (\pi/2)c_1P^2$, where c_1 is the first Mooney–Rivlin coefficient. In a pure-shear strip, the grip stretch therefore fixes P, and finite-element calculations support both this parameter-free amplitude and the compensated-Jacobian prediction. The constraint also permits a regular $O(r)$ crack-parallel motion set by specimen-scale matching. After this motion is separated, the in-plane field contains an $r^{5/4}$ residual whose angular equation admits a specimen-selected homogeneous member. Core and angular refinement of the strip fields recovers both the exact-axis 5/4 exponent and its parameter-free amplitude to within 1.3%. The closed normal-opening sector gives the half-odd radial spectrum and a conserved symplectic pairing. The calculation shows how a constitutive term that is subleading in the near-tip energy can nevertheless control the local kinematics, a mechanism that can be sought in other stiffening soft networks.

1 Introduction

Crack growth and energy dissipation in soft solids are controlled by the highly deformed region near the crack tip. The development of tough soft materials, particularly hydrogels [1–3], has therefore increased the need for quantitative near-tip mechanics [4, 5]. The crack-tip field connects specimen-scale loading to the local deformation that drives rupture. Continuum crack-tip fields are singular, while fracture and dissipation cut off that singularity in a real material. The asymptotic field describes the intermediate region between the remote loading and this process zone.

Most analytical crack-tip fields for soft sheets are restricted to generalized neo-Hookean solids, $W = W(I_1)$. Foundational finite-strain studies established the basic crack-tip structures [6–12]. Krishnan, Hui and Long developed the incompressible plane-stress theory most relevant to soft sheets [13, 14]. Long and Hui later reviewed this framework [15], and Liu and Moran extended it to fiber-reinforced sheets [16, 17]. These hodograph formulations rely on $W = W(I_1)$ and do not extend directly to a general constitutive law. The Mooney–Rivlin (MR) energy

$$W = c_1(I_1 - 3) + c_2(I_2 - 3) \tag{1}$$

is the simplest widely used model beyond that class [18–21]. The analytical plane-stress theories cited above do not include it. Han and Li instead used finite elements to quantify apparent stress indices at finite distance from the tip and noted the absence of an asymptotic Mooney–Rivlin field [22]. In incompressible plane strain, $I_1 = I_2$, so the Mooney–Rivlin energy reduces to a neo-Hookean form. The crack-tip field then has a single $r^{1/2}$ intensity factor [10, 23, 24]. This reduction is specific to plane strain. In the plane-stress problem considered here, the second invariant remains active. We study $c_1 > 0$, $c_2 > 0$ and use $c_2 = 0$ as the neo-Hookean control.

We apply the symplectic (Hamiltonian) formulation of elasticity to radial crack-tip asymptotics, using $\xi = \ln r$ as the evolution coordinate. A power law r^{Λ} then becomes the exponential mode $e^{\Lambda\xi}$, so the classical crack-tip hierarchy [25, 26] becomes a spectrum of the radial evolution [27]. Spatial Hamiltonian formulations pair a displacement trace with its generalized traction [27–29]. Here the variational reduction identifies the deformed-position trace on a material circle and the weighted nominal traction $r\mathbf{P}\mathbf{e}_r$ as the canonical pair. This viewpoint is especially useful when a constitutive term becomes a constraint. Its reaction remains in the traction variable even when the constrained kinematics suppress its leading energetic contribution. Related finite-strain incremental symplectic methods have been used for instabilities in layered neo-Hookean structures [30].

Within this framework, dominant balance shows that the plane-stress c_2 term imposes a near-tip kinematic constraint and drives the local state toward uniaxial tension. The leading field has an $r^{1/2}$ opening, angle-independent stretch magnitudes, an angle-independent compensated Jacobian, and $G = (\pi/2)c_1P^2$, where $y_2 \sim Pr^{1/2}\sin(\theta/2)$. Pure-shear strip calculations test the resulting parameter-free amplitude and Jacobian predictions. Refinement toward the tip also recovers the exact-axis $5/4$ residual exponent and amplitude. The constraint leaves a regular contour motion $C_s s = C_s r \sin^2(\theta/2)$, whose coefficient must be supplied by the outer specimen. Once that motion is separated, the harmonic opening and the constraint predict an $r^{5/4}$ in-plane residual. Its angular equation has an analytic-axis member $g(\theta)$ and a homogeneous member whose amplitude is supplied by matching. The constrained linearization also contains a closed normal-opening sector with a half-odd spectrum and a conserved symplectic pairing. In the limit $c_2 \to 0$, the opening and energy relation reduce to those of Long, Krishnan and Hui [14]. On the selected $F = 0$, analytic-axis representative, the first material correction closes explicitly. Farther along that formal hierarchy, a restricted nonlinear source resonates with the opening operator and requires a logarithmic opening companion. Figure 1 summarizes the specimen, radial state, and constrained tip geometry.

Section 2 reduces the plane-stress sheet to a two-dimensional energy and derives its nominal stress. Section 3 constructs the radial Hamiltonian action, identifies the canonical state, and derives the conserved pairing for the constrained linearization. Section 4 obtains the constraint-active tip field, its physical null motion, the $r^{5/4}$ residual, and the first material correction. Section 5 develops the closed opening spectrum, its symplectic pairing, and the higher-order resonance. Section 6 derives parameter-free relations and tests them in pure-shear finite-element calculations. Section 7 evaluates the energy release rate, after which the discussion connects the local state to failure, specimen-scale matching, and other stiffening networks.

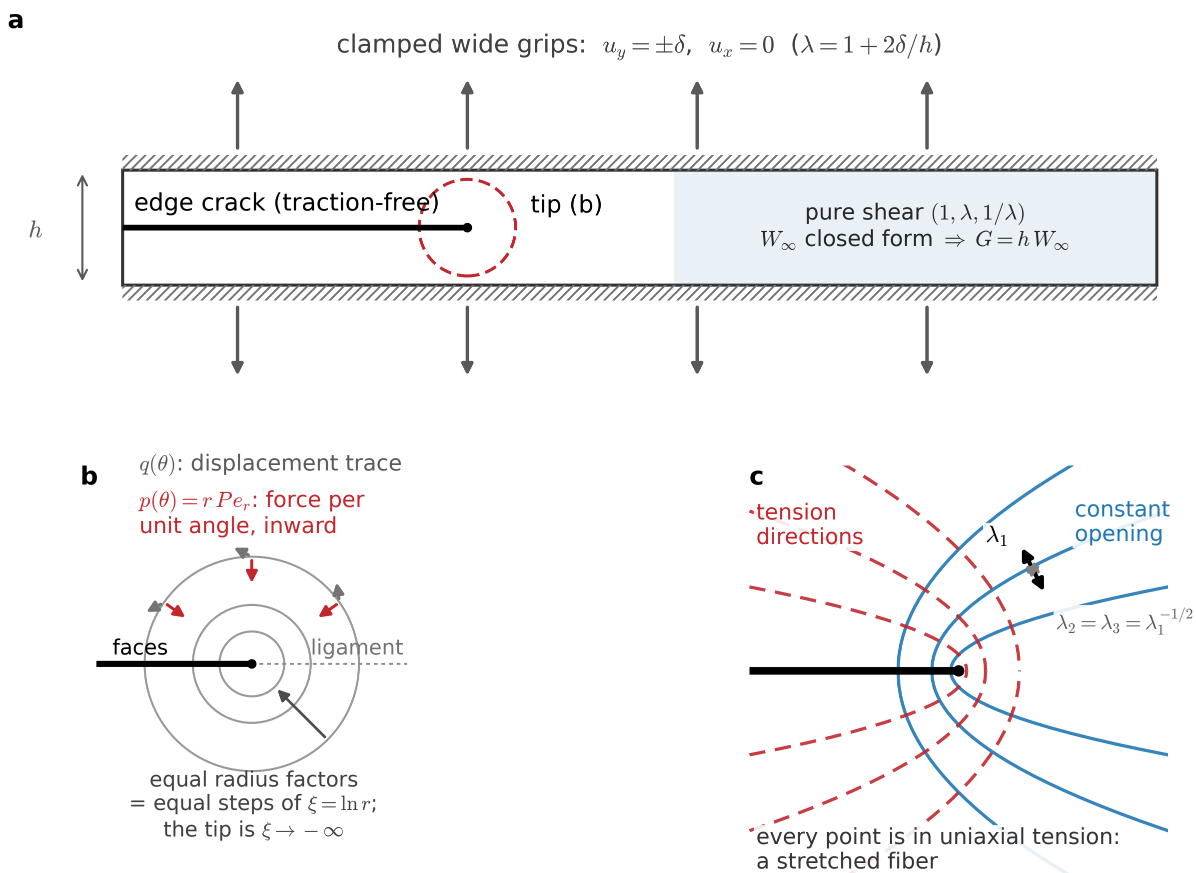

Figure 1: Specimen, radial state, and constrained tip field. (a) The Rivlin–Thomas pure-shear strip [31]. The remote state is $(1, \lambda, 1/\lambda)$, with $\lambda = 1+2\delta/h$ and $G = hW_\infty$. (b) A circular contour carries the deformed-position trace $\mathbf{q}(\theta)$ and momentum $\mathbf{p}(\theta) = r\,\mathbf{P}\mathbf{e}_r$. Equal radial factors correspond to equal increments of $\xi = \ln r$. (c) The constrained tip state. The maximum stretch λ_1 follows the local tension direction (red), while the transverse stretches are equal. Blue curves show constant opening, $y_2 = P\sqrt{s}$ with $s = r\sin^2(\theta/2)$, along which the constraint reaction is transported. Panels (b,c) show the local analytical construction. These fields are not imposed on the strip.

2 The sheet as a two-dimensional solid

Consider a thin sheet of the material (1) deformed in its plane, with the crack tip at the origin of polar coordinates (r, θ) and the crack faces along $\theta = \pm\pi$. Plane stress means the faces of the sheet are traction-free through the thickness. Incompressibility ties the thickness stretch to the in-plane areal change, $\lambda_3 = J^{-1}$, where $J = \det \mathbf{F}$ and $\mathbf{F} = \partial\mathbf{y}/\partial\mathbf{X}$. Thus the sheet thins wherever it is stretched in area. Substituting λ_3 eliminates the thickness direction. The three-dimensional invariants become $I_1 = \mathrm{tr}(\mathbf{F}^\top\mathbf{F}) + J^{-2}$ and $I_2 = J^2 + \mathrm{tr}(\mathbf{F}^\top\mathbf{F})J^{-2}$ with $\mathrm{tr}(\mathbf{F}^\top\mathbf{F}) = \mathbf{F}:\mathbf{F}$. The sheet is then governed by the unconstrained two-dimensional energy

$$W = c_1\Big(\mathrm{tr}(\mathbf{F}^\top\mathbf{F}) + J^{-2} - 3\Big) + c_2\Big(J^2 + \mathrm{tr}(\mathbf{F}^\top\mathbf{F})J^{-2} - 3\Big). \tag{2}$$

The corresponding first Piola–Kirchhoff stress is

$$\mathbf{P} = 2c_1\Big(\mathbf{F} - J^{-2}\mathbf{F}^{-\top}\Big) + 2c_2\Big(J^{-2}\mathbf{F} + \big(J^2 - J^{-2}\mathbf{F}:\mathbf{F}\big)\mathbf{F}^{-\top}\Big). \tag{3}$$

This is the force per unit *reference* area transmitted across an interface in the sheet. It is also the stress used in both the flux integrals and the finite-element calculations. That (3) coincides with the in-plane block of the three-dimensional stress is the result of a pressure elimination. In three dimensions, incompressibility introduces a pressure p, and the plane-stress condition $P_{33} = 0$ determines it as $p = \lambda_3 \, \partial W_{3\mathrm{D}} / \partial \lambda_3$, where $W_{3\mathrm{D}}$ is the unconstrained three-dimensional energy (1). Differentiating the reduced energy (2) then produces, through the substitution $\lambda_3 = J^{-1}$, the chain-rule term $-\lambda_3 (\partial W_{3\mathrm{D}} / \partial \lambda_3) \, \mathbf{F}^{-\top}$, which is exactly the pressure term of the three-dimensional stress. The true (Cauchy) stress follows as $\boldsymbol{\sigma} = \mathbf{P}\mathbf{F}^{\top}$. No factor of $1/J$ appears because the full three-dimensional determinant is unity. Here J is the in-plane *areal* Jacobian, not a volume change.

3 Crack-tip asymptotics as radial Hamiltonian dynamics

The symplectic (Hamiltonian) formulation of elasticity, with one spatial coordinate playing the role of time, goes back to Zhong and co-workers [28, 29]. Symplectic eigenfunction expansions have also been used for crack and notch problems in *linear* elasticity, where stress-intensity factors appear as expansion coefficients [27]. Related finite-strain incremental symplectic methods have been developed for wrinkling instabilities in layered neo-Hookean structures [30]. We use the spatial Hamiltonian frame with $\xi = \ln r$ as the radial coordinate of a nonlinear crack tip.

We describe the radial variation of fields on circles $r = \text{const}$ using the pseudo-time

$$\xi = \ln r, \tag{4}$$

so that the crack tip corresponds to $\xi \to -\infty$. Shrinking the circle by a fixed factor gives a fixed decrement of ξ. The exponentials $e^{\Lambda\xi} = r^{\Lambda}$ are the power laws of crack-tip mechanics. Radial derivatives become $\partial_r = e^{-\xi}\partial_\xi$, and the arc element on the circle is $e^{\xi}\mathrm{d}\theta$.

In the variables of (4), the energy stored between two circles is

$$\mathcal{A} = \iint W \, r \, \mathrm{d}r \, \mathrm{d}\theta = \int \Big(\int_{-\pi}^{\pi} W \, e^{2\xi} \, \mathrm{d}\theta \Big) \, \mathrm{d}\xi =: \int \mathcal{L}\big(\mathbf{q}, \partial_\xi \mathbf{q}\big) \, \mathrm{d}\xi. \tag{5}$$

This is a classical action with ξ as time and the trace $\mathbf{q}(\theta)$ of the deformed position $\mathbf{y}$ on the circle as the configuration.

The momentum conjugate to $\mathbf{q}$ is

$$p_i = \frac{\delta \mathcal{L}}{\delta(\partial_\xi q_i)} = e^{2\xi} \, P_{ir} \, e^{-\xi} = r \, P_{ir}, \tag{6}$$

the r-weighted radial nominal traction ($i \in \{1, 2\}$ labels Cartesian components, and P_{ir} is the radial component of the stress (3) in polar coordinates). It is the force per unit angle that the material outside the circle transmits inward. The area weight and the radial-gradient transformation leave one power of r.

The Euler–Lagrange equations of (5) are the equilibrium equations. Applying the Legendre transform $\mathcal{H} = \int \mathbf{p} \cdot \partial_\xi \mathbf{q} \, \mathrm{d}\theta - \mathcal{L}$ converts them into $\partial_\xi \mathbf{q} = \delta\mathcal{H}/\delta\mathbf{p}$, $\partial_\xi \mathbf{p} = -\delta\mathcal{H}/\delta\mathbf{q}$, which are first order in ξ.

Elasticity has no intrinsic length. Concretely, for a quadratic energy the $e^{2\xi}$ area weight in (5) cancels against the $e^{-2\xi}$ scaling of the squared gradient. The resulting Hamiltonian is autonomous in ξ. For the full Mooney–Rivlin energy, whose terms have different homogeneities in the gradient, no such cancellation holds for the unweighted state. Autonomy is recovered for the linearization about the scale-similar leading orbit in the weighted variables of Sec. 5.

For quadratic $\mathcal{H}$ Hamilton's equations are linear,

$$\frac{\mathrm{d}\mathbf{V}}{\mathrm{d}\xi} = \mathbf{H}\,\mathbf{V}, \qquad \mathbf{V} = \begin{bmatrix}\mathbf{q}\\ \mathbf{p}\end{bmatrix}, \qquad \mathbf{H} = \mathbf{J}\,\nabla^2\mathcal{H}, \quad \mathbf{J} = \begin{bmatrix}\mathbf{0} & \mathbf{I}\\ -\mathbf{I} & \mathbf{0}\end{bmatrix}, \tag{7}$$

and $\mathbf{JH} = -\nabla^2\mathcal{H}$ is symmetric. This gives the symplectic identity $\mathbf{JH} = -\mathbf{H}^\top\mathbf{J}$.

For a linear material, the eigenproblem of $\mathbf{H}$ is the Williams problem, which gives the classical power-series catalog of linear-elastic crack-tip fields. The same expansion is recovered in the symplectic literature [27, 28] and can also be connected directly to Muskhelishvili complex potentials [26]. For finite strain, the leading orbit is nonlinear, but its second variation again produces a Jacobi system. In the present problem the normal-opening component decouples at the leading radial grade and can be solved without an angular truncation. The same construction shows how the constraint reaction enters the coupled in-plane sector. Because the weighted linearization is autonomous in ξ, its modes are exponentials in ξ, or powers r^Λ. The face conditions select their angular profiles, while finite energy selects the admissible half of the spectrum. The closed normal-opening sector below recovers the half-odd harmonic family. The subdominant I_2 stress then forces this linearized hierarchy at radial weights separated by half powers, producing the ordering derived in Sec. 4.

The symplectic identity gives a radial reciprocity relation. For any two solutions whose angular boundary terms vanish, the bilinear form $\Omega(\mathbf{V},\mathbf{W}) = \int(\mathbf{q}_V\cdot\mathbf{p}_W - \mathbf{q}_W\cdot\mathbf{p}_V)\,\mathrm{d}\theta$ is independent of ξ. The boundary terms vanish on traction-free crack faces. Mode-I symmetry reduces the integral to $[0,\pi]$. Section 5 uses this pairing as a solvability condition and identifies the adjoint opening modes. The structure parallels the reciprocity between stress-intensity factors and weight functions in linear fracture mechanics. The energy flux in Sec. 7 is evaluated separately from the classical J-integral.

The same structure survives when the energy contains a constraint. If a stiff term of W enforces a kinematic condition $\mathcal{C} = 0$ at the tip, with action multiplier χ, the action becomes

$$\mathcal{A}[\mathbf{y},\chi] = \iint \big(W_1(\mathbf{F}) + \chi\,\mathcal{C}(\mathbf{F})\big)e^{2\xi}\,\mathrm{d}\theta\,\mathrm{d}\xi. \tag{8}$$

Here W_1 is the surviving elastic energy. Stationarity in $(\mathbf{y},\chi)$ gives the constrained equilibrium and the constraint. Writing $\mathbf{y} = \mathbf{y}^0 + \mathbf{u}$ and $\chi = \chi^0 + \varphi$ about a leading orbit, the second variation is the quadratic functional

$$\delta^2\mathcal{A} = \iint \big(\delta\mathbf{F} : \mathbb{A}^0 : \delta\mathbf{F} + 2\,\varphi\,\mathcal{C}^0_{\mathbf{F}} : \delta\mathbf{F}\big)e^{2\xi}\,\mathrm{d}\theta\,\mathrm{d}\xi, \qquad \mathbb{A}^0 = W_1''(\mathbf{F}^0) + \chi^0\,\mathcal{C}''(\mathbf{F}^0), \tag{9}$$

whose stationarity conditions are the linearized equations. Three facts follow. First, $\mathbb{A}^0$ is a Hessian, so the linearized equations form a Jacobi system that is formally self-adjoint in $(\mathbf{u},\varphi)$. Second, the multiplier increment φ carries no ξ-derivative, so its momentum vanishes. The first-order equations are therefore differential-algebraic. The reaction enters through the incremental momenta $\boldsymbol{\pi}$, which are built from $\mathbb{A}^0 : \delta\mathbf{F} + \varphi\,\mathcal{C}^0_{\mathbf{F}}$. The pairing needs no separate multiplier slot. Third, self-adjointness gives the Lagrange identity. For any two solutions of the linearized system,

$$\frac{\mathrm{d}}{\mathrm{d}\xi}\int_0^\pi \big(\mathbf{u}\cdot\bar{\boldsymbol{\pi}} - \bar{\mathbf{u}}\cdot\boldsymbol{\pi}\big)\,\mathrm{d}\theta = \Big[\mathbf{u}\cdot\bar{\boldsymbol{\sigma}}_\theta - \bar{\mathbf{u}}\cdot\boldsymbol{\sigma}_\theta\Big]_0^\pi, \tag{10}$$

with $\boldsymbol{\sigma}_\theta$ the incremental angular traction. The volume terms cancel by the symmetry of $\mathbb{A}^0$, and the reaction terms cancel because both solutions satisfy the constraint row. The left side is the incremental pairing Ω. It is conserved whenever the endpoint concomitant vanishes. On eigen-solutions, Ω carries the factor $e^{(\Lambda+\Lambda'-\sigma)\xi}$. A nonzero pairing therefore requires $\Lambda + \Lambda' = \sigma$, where σ is set by the weights of the paired block. Any constrained-limit operator for the sheet must inherit this structure. We use it here on the closed normal-opening sector of Sec. 5, where the scalar reduction follows directly from the leading constrained second variation. Section 7 uses the resulting duality counting.

To keep reaction coefficients unambiguous, we fix the constraint normalization $\mathcal{C} = J^4 - |\nabla y_2|^2$ and denote its action multiplier by χ. Rescaling $\mathcal{C}$ would rescale χ inversely, so coefficients of the reaction field refer to this convention. The coefficient C_s introduced below labels the first analytic motion along the opening contours. We retain it in the physical map and separate it as the determinant-null function $F(y_2)$ when deriving the $r^{5/4}$ residual. For later radial bookkeeping, $F = 0$ is used as one base point in this local null family. That choice is not a specimen-level condition. A nonzero C_s changes the coupled subleading problem, but not the normal-opening sector or the leading energy flux.

4 The I_2 term becomes a constraint at the tip

Incompressible plane stress eliminates the thickness stretch (Sec. 2), leaving the unconstrained functional (2) of the in-plane deformation gradient. At a material point with dominant stretch λ_1 the energy splits as $W \approx c_1\lambda_1^2 + c_2\lambda_1^2(\lambda_2^2 + \lambda_3^2)$. Near the tip $\lambda_1^2 \sim 1/r$ diverges. Incompressibility already fixes the *product* of the transverse stretches, $\lambda_2\lambda_3 = \lambda_1^{-1}$. The c_2 term additionally penalizes the sum $\lambda_2^2 + \lambda_3^2$ with a stiffness that grows without bound, and at fixed product that sum is smallest when $\lambda_2 = \lambda_3$. The two conditions together force the field onto the manifold

$$\lambda_2 = \lambda_3 = \lambda_1^{-1/2}. \tag{11}$$

Within the constrained outer region, each material point therefore approaches the state of a stretched fiber, or an incompressible bar in uniaxial tension. On this manifold I_2 grows only linearly in λ_1, while I_1 grows quadratically. The leading elastic response is therefore neo-Hookean-dominated, even though the I_2 term controls the transverse kinematics through the constraint.

The constrained zone is the region where the c_2 penalty dominates the c_1 elasticity. Its off-manifold stiffness grows as $c_2\lambda_1^2 = c_2P^2/(4r)$, where $\lambda_1 = (P/2)\,r^{-1/2}$ from Eq. (23). It overtakes the $O(c_1)$ elastic stiffness for $r \lesssim r_* = P^2c_2/(4c_1)$. Here P is the opening amplitude introduced below, and r_* is a scale estimate rather than a sharp boundary. It shrinks to nothing as $c_2 \to 0$ and deepens as c_2/c_1 grows. The material-ratio study in Sec. 6 is consistent with this crossover picture.

The $c_2 \to 0^+$ limit is therefore singular. The constrained zone empties, $r_* \to 0$, while at any fixed $r < r_*$ the kinematics remain uniaxial. The two limits do not commute: $\lim_{c_2\to 0^+}\lim_{r\to 0}(\lambda_2/\lambda_3) = 1$, whereas $\lim_{r\to 0}\lim_{c_2\to 0^+}(\lambda_2/\lambda_3) \neq 1$ in general. What the limit preserves continuously is the opening field and the energy relation of Sec. 7. As $c_2 \to 0^+$, the radial interval over which the constraint, the Jacobian plateau, and the associated in-plane residual can be observed contracts to zero. This is why the $c_2 = 0$ control passes the opening tests and fails the kinematic ones in Sec. 6.

At leading order, the in-plane equilibrium equation reduces to the pointwise kinematic identity (here and throughout, $J = \det \mathbf{F}$ is the in-plane areal Jacobian of Sec. 2)

$$J^4 = |\nabla y_2|^2. \tag{12}$$

This identity sets the areal Jacobian through the opening gradient but does not set the entire in-plane map. The dominant balance can be seen directly from (3). Write $\mathbf{b} = \nabla y_2$, $L = |\mathbf{b}|$,

$\widehat{\mathbf{t}} = \mathbf{b}/L$, and $\widehat{\mathbf{n}} = \mathbf{b}^{\perp}/L$, where $\mathbf{b}^{\perp} = (b_2, -b_1)$. Decompose $\nabla y_1 = q\widehat{\mathbf{t}} + (J/L)\widehat{\mathbf{n}}$. The exact normal component of the first stress row contains

$$\frac{1}{2}\mathbf{P}_1 \cdot \widehat{\mathbf{n}} = c_1\left(\frac{J}{L} - \frac{L}{J^3}\right) + c_2\frac{L}{J^3}\left(J^4 - L^2 - q^2\right). \tag{13}$$

For $L = O(r^{-1/2})$, $J = O(r^{-1/4})$, and $|\nabla y_1|/L \to 0$, a leading defect $\mathcal{C} = J^4 - L^2 = O(r^{-1})$ would make the $c_2\mathcal{C}$ stress divergence $O(r^{-7/4})$, more singular than all remaining row-one terms. The leading row is $\nabla \cdot [\mathcal{C}J^{-3}\mathbf{b}^{\perp}] = 0$, or transport of $\mathcal{C}/J^3$ along the y_2 level sets. Traction freedom sets this quantity to zero where each level set reaches the crack face, giving $\mathcal{C} = 0$ and hence (12). Within this formal outer argument, the symmetry-axis characteristic is selected by regular continuation. After the determinant-null contour motion is subtracted, $q = O(r^{1/4})$. Retaining $C_s s$ in the physical map gives $q = O(1)$. With either bookkeeping choice, $q = o(L)$ and the leading second-row stress is $\mathbf{P}_2 = 2c_1\nabla y_2 + o(r^{-1/2}) = 2c_1\nabla y_2 + o(|\nabla y_2|)$, so

$$\Delta y_2 = 0, \qquad y_2(\theta = 0) = 0, \qquad \partial_\theta y_2(\theta = \pi) = 0. \tag{14}$$

Although the on-manifold c_2 energy is only $O(r^{-1/2})$, compared with the $O(r^{-1})$ c_1 energy, its off-manifold derivative supplies the dominant constraint reaction. In particular, its defect part has the row-one reaction form

$$2c_2J^{-3}\mathcal{C}\,\mathbf{b}^{\perp} = \chi_{\text{pen}}\,\mathcal{C}_{\nabla y_1}, \qquad \chi_{\text{pen}} = \frac{c_2}{2}J^{-6}\mathcal{C}, \tag{15}$$

where $\mathcal{C}_{\nabla y_1} = 4J^3\mathbf{b}^{\perp}$. Here χ_{pen} is the finite-compliance defect reaction, not the total constrained-action multiplier: $\mathcal{C} = 0$ on the base while χ^0 is generally nonzero. The exact row decompositions, both radial power counts, face argument, and assumptions are given in the ESI.

Equation (12) fixes only the $\widehat{\mathbf{n}}$ component of ∇y_1: $J = L(\nabla y_1 \cdot \widehat{\mathbf{n}})$ gives $\nabla y_1 \cdot \widehat{\mathbf{n}} = L^{-1/2}$ on the orientation-preserving branch. It leaves the $\widehat{\mathbf{t}}$ component free. Indeed, for any differentiable F,

$$\det\left(\nabla y_1 + F'(y_2)\nabla y_2, \nabla y_2\right) = J. \tag{16}$$

Under Mode-I parity the first nonconstant analytic null addition is $F(y_2) = (C_s/P^2)y_2^2 + \cdots$, whose leading form is $C_s s$, with $s = r\sin^2(\theta/2)$. To determine the first in-plane residual, write $y_2 = P\,r^{a_2}f(\theta)$ and $\bar{y}_1 := y_1 - c_0 - F(y_2) = Qr^{a_1}g(\theta)$, where the scalar amplitude P is not to be confused with the stress tensor $\mathbf{P}$ of (3). Because $F(y_2)$ is exactly determinant-null, the two sides of (12) have the radial forms

$$J = PQr^{a_1+a_2-2}\big(a_1 f'g - a_2 fg'\big), \qquad |\nabla y_2|^2 = P^2r^{2a_2-2}\big(a_2^2f^2 + f'^2\big). \tag{17}$$

Matching the powers of r in (17) under (12) gives $4(a_1 + a_2 - 2) = 2a_2 - 2$, or $2a_1 + a_2 = 3$. At leading order the normal equilibrium is governed by the surviving neo-Hookean (c_1) response. On the constraint manifold, I_2 grows only linearly in λ_1 while I_1 grows quadratically, so the c_2 contribution is subdominant in this equation. The scalar opening equation is therefore harmonic. Mode-I symmetry and the traction-free face select $a_2 = 1/2$ and $f(\theta) = \sin(\theta/2)$, as recovered independently by the normal-opening spectrum in Sec. 5. Substitution into $2a_1 + a_2 = 3$ fixes $a_1 = 5/4$ for the in-plane residual. The leading measurement-space expansion is

$$\begin{aligned} y_2 &= P\,r^{1/2}\sin(\theta/2) + \cdots, \\ y_1 &= c_0 + F(y_2) + P^{-1/2}\,r^{5/4}\,g(\theta) + \cdots \\ &= c_0 + C_s s + P^{-1/2}\,r^{5/4}\,g(\theta) + \cdots. \end{aligned} \tag{18}$$

Thus the 5/4 power follows from two analytical ingredients: the harmonic 1/2 opening and the constraint (12). The angular function $g(\theta)$ follows from the coefficient balance below.

The local constraint does not determine C_s. The outer boundary-value problem must supply this regular motion. On the crack face, $s = r$, so

$$y_1 - c_0 = C_s r + A r^{5/4} + \cdots, \qquad y_2 = P r^{1/2} + \cdots, \qquad A = P^{-1/2} g(\pi). \tag{19}$$

Here "opening" means the normal displacement at a fixed reference distance from the tip. Mode-I symmetry gives a leading face separation $2P\sqrt{r}$, independent of C_s. The coefficient C_s instead shifts the crack-parallel coordinate, much as a regular outer coefficient supplements a singular field in linear fracture mechanics. The residual is defined after subtracting this determinant-null motion. This decomposition does not set the specimen's C_s to zero. In the physical field, the two terms in Eq. (19) must be retained together.

After the null function $F(y_2)$ has been separated, the in-plane profile g obeys the first-order equation

$$\tfrac{5}{4}\, f' g - \tfrac{1}{2}\, f g' = 2^{-1/2}, \qquad f = \sin(\theta/2), \tag{20}$$

which gives $g(0) = 4\sqrt{2}/5$ at the symmetry axis and $g'(\pi) = -\sqrt{2}$ at the crack face. These endpoint values do not determine the coefficient of the homogeneous solution $g_h = C_h f^{5/2}$, corresponding to the shear $y_1 \to y_1 + P^{-1/2} C_h s^{5/4}$ along the tension lines. It vanishes together with its first two derivatives at the axis and has $g_h'(\pi) = 0$. The general solution is

$$g(\theta) = f(\theta)^{5/2}\Big[g(\pi) + \sqrt{2}\int_\theta^\pi f(\theta')^{-7/2}\,\mathrm{d}\theta'\Big]. \tag{21}$$

Near the axis the bracket contributes $\frac{4\sqrt{2}}{5} f^{-5/2}$, analytic even terms, and a constant. The constant multiplies $f^{5/2} \sim (\theta/2)^{5/2}$, a term whose third derivative diverges. Motivated by smooth continuation from the intact ligament, we select an angular field that is analytic across the symmetry axis. This removes the fractional-power term and leaves a branch with even integer powers of θ. Under this intact-axis assumption,

$$g(\pi) = -\sqrt{2}\, A_f = 2.0333\ldots. \tag{22}$$

Here $A_f = -1.4378$ is the finite part of the tail integral at the axis. It is a one-dimensional quadrature and is the only numerical ingredient in the selected profile. A homogeneous coefficient could survive through a shrinking angular layer at the symmetry axis, so the intact-axis condition is a matching assumption rather than an existence theorem. The numerical test of the 5/4 class and its exact-axis amplitude is discussed in Sec. 6. The same $s^{5/4}$ homogeneous residual belongs to the half-power space of Sec. 5.

The factor $P^{-1/2}$ normalizes the residual on this branch. Rescaling this factor and g inversely leaves their product unchanged. It is not the coefficient C_s of the distinct physical null direction. With g normalized by (20), the $r^{5/4}$ residual amplitude on this branch scales as $P^{-1/2}$.

The leading principal-stretch magnitudes are independent of θ,

$$\lambda_1 \sim \frac{P}{2}\, r^{-1/2}, \qquad \lambda_2 \sim \lambda_3 \sim \sqrt{\frac{2}{P}}\, r^{1/4}. \tag{23}$$

Only the principal directions rotate. These asymptotics hold in an annulus,

$$t_\mathrm{s} \ll r \ll \min(r_*, r_{I_2}), \qquad r_* = \frac{P^2 c_2}{4 c_1}, \quad r_{I_2} \sim P^2 \Big(\frac{c_1}{c_2}\Big)^2. \tag{24}$$

The lower bound is the sheet thickness t_s. Below it, the reduction of Sec. 2 fails and the field becomes three-dimensional. The subscript distinguishes the thickness from the confocal coordinate t used below. The upper bound is the smaller of the constrained-zone edge r_* and the scale r_{I_2} beyond which the on-manifold I_2 correction in Eq. (25) is no longer small. For $c_2 \lesssim c_1$, the binding scale is r_*. For $c_2/c_1 = 3$, it is r_{I_2}, consistent with the slower convergence of the free opening exponent at that ratio in Sec. 6. In the pure-shear strip, $r_* \sim 0.3\,h$ at $\lambda = 1.6$ and $c_1 = c_2$. It grows toward h by $\lambda = 2.2$ and also grows with c_2/c_1. The window is about a decade wide when the sheet thickness is a few percent of its height. It narrows for thicker sheets or smaller c_2/c_1. These bounds determine the radial range over which the constrained residual and the null background must be separated.

To organize the later corrections, choose $F = 0$ as a bookkeeping base point in the determinant-null family. On this representative the on-manifold I_2 stress is smaller than the neo-Hookean response by $(c_2/c_1)\lambda_1^{-1} = O(r^{1/2})$. Formal radial bookkeeping therefore places the first paired correction in the slots

$$\begin{aligned} y_2 &= P\,r^{1/2} f(\theta) + \frac{c_2}{c_1}\,r\,v(\theta) + O(r^{3/2}), \\ y_1 &= P^{-1/2} r^{5/4} g(\theta) + \frac{c_2}{c_1} P^{-3/2} r^{7/4} w(\theta) + O(r^{9/4}). \end{aligned} \tag{25}$$

Equation (25) records the radial and dimensional ordering about that base point, not the field selected by a particular specimen. Their global endpoint completion is not needed for the claims below. If $C_s \neq 0$, its $O(1)$ gradient reorders these subleading balances, so Eq. (25) must not be transferred unchanged to a retained-C_s branch.

The first correction on this representative is solved, with opening profile

$$v(\theta) = -\frac{2}{3}\sin(\theta/2).$$

The in-plane shear $w(\theta)$ is slaved to it by the constraint, with $w(0) = 4\sqrt{2}/21$ at the axis. Retaining the full c_2 term of Eq. (2) before enforcing $\mathcal{C} = 0$ fixes the multiplier convention. In that convention, $\delta\chi = c_2 P^{-4} r^2 p(\theta)$, with endpoint values $p(0) = -256/15$ and $p(\pi) = 25 g(\pi)^2/4$. They enforce the total crack-face traction at this grade. Both homogeneous directions of the rung are fixed within it. The shear direction $f^{7/2}$ is excluded by analyticity at the axis, and the reaction direction $f^{5/2}$ is selected by the total crack-face traction. On this $F = 0$, analytic-axis representative the rung therefore contains no additional local amplitude. Exact symbolic identities in the repository verify its field equations, constraint, and total tractions, and independent arbitrary-precision continuation checks the endpoint evaluations. The outgoing contribution this rung generates at the next grade is obtained exactly.

The closed normal-opening sector admits further harmonics beyond the leading member. The constraint also admits analytic shears along the opening level sets, and Sec. 5 organizes both families. Those level sets form one family of the confocal-parabola system in Fig. 1. With $s = (r - r\cos\theta)/2 = r\sin^2(\theta/2)$, the leading opening is $y_2 = P\sqrt{s}$. Its level sets $s = \text{const}$ are the characteristics along which the reaction stress is transported. The orthogonal family $t = \text{const}$, with $t = (r + r\cos\theta)/2 = r\cos^2(\theta/2)$ the confocal partner of s, gives the tension trajectories, tangent to the local maximum-stretch direction. This confocal geometry gives a physical picture of the constraint: opening is constant and the reaction is transported along one family, while tension follows the orthogonal family.

5 Symplectic opening spectrum and higher-order outlook

At the leading radial grade of the constrained second variation, the normal opening decouples from the in-plane displacement and constraint reaction. Its scalar equation is therefore independent of the determinant-null contour motion at this grade. A specimen-selected $C_s s$ term remains part of the physical base map and changes the coupled subleading operator, but not the normal-opening equation derived here. Within this closed scalar sector the reduction below is exact: it follows without an angular truncation and gives the opening spectrum and its conserved pairing. At later grades, the in-plane and reaction components re-enter as a coupled problem.

Let $\xi = \ln r$. Because the leading in-plane residual and opening fields differ by the radial factor $r^{3/4}$, a convenient pencil label Λ represents physical increments

$$\delta y_1 \propto r^{\Lambda} a(\theta), \qquad \delta y_2 \propto r^{\Lambda-3/4} b(\theta). \tag{26}$$

The closed normal-opening sector obeys the scalar harmonic equation

$$-b'' = (\Lambda - \tfrac{3}{4})^2 b, \qquad b(0) = 0, \qquad b'(\pi) = 0. \tag{27}$$

Thus the physical opening powers are $\nu = \Lambda - \frac{3}{4} = \frac{1}{2}, \frac{3}{2}, \frac{5}{2}, \ldots$, with angular profiles $\sin(\nu\theta)$. The first member is the leading opening derived in Sec. 4. The $\nu = 3/2$ member is the opening seed of the B sector. As with higher Williams coefficients in linear fracture, its amplitude is supplied by the outer specimen rather than by the local eigenproblem.

For an eigenfunction in this sector, restore the full radial field

$$u_2(\xi, \theta) = e^{\nu\xi} b(\theta), \qquad \nu = \Lambda - \tfrac{3}{4}, \qquad \tau_2 := \partial_\xi u_2, \tag{28}$$

where τ_2 is the opening momentum apart from the common $2c_1$ normalization. For two full opening fields, the Wronskian current

$$\Omega_{\mathrm{op}}(\mathbf{V}, \mathbf{W}) = \int_0^{\pi} \big(u_{2V}\tau_{2W} - u_{2W}\tau_{2V}\big)\,\mathrm{d}\theta \tag{29}$$

is independent of ξ after using $\partial_\xi^2 u_2 + \partial_\theta^2 u_2 = 0$ and integrating by parts. The endpoint term vanishes under the mixed conditions in Eq. (27). For power-law solutions, the current is proportional to $e^{(\nu+\nu')\xi}$. A nonzero conserved pairing therefore requires $\nu' = -\nu$, or $\Lambda' = \frac{3}{2} - \Lambda$. The paired physical opening powers are opposites. This conserved opening-mode pairing supplies the usual Fredholm condition for forced opening corrections. The homogeneous opening spectrum contains eigenvalues at $\Lambda = 5/4$ and $9/4$. On the same $C_s = 0$ representative, the formal stationary-background calculation reaches $\Lambda = 11/4$, but its outgoing target leaves the finite-action endpoint class. We therefore retain it only as an algebraic checkpoint, not as a matched physical mode.

At the pencil label $\Lambda = 13/4$, corresponding to the opening power $r^{5/2}$, the opening operator is exactly resonant. The source must be orthogonal to the kernel $\sin(5\theta/2)$. On the selected $C_s = 0$ branch, the numerically converged projection of the restricted source that couples the first material correction to the stationary background is nonzero. That formal opening coefficient therefore requires a contribution $r^{5/2}\log(r/r_0)\sin(5\theta/2)$. The complete same-grade source, the coupled response, and the physically selected net logarithmic amplitude remain open.

The constraint also admits analytic shears along the opening level sets, $y_1 \mapsto y_1 + \sum_{k\geq 1} Q_k s^k$. The $k = 1$ member is the physical leading-null term $C_s s$ already displayed in Eq. (18). It is not a gauge. For $k \geq 2$ these seeds are G-quiet at leading order. Their reaction and opening companions, and the specimen amplitudes B and Q_k, belong to the coupled matching problem.

Figure 2 summarizes the constraint physics in the local field and the way the radial Hamiltonian structure organizes its first corrections.

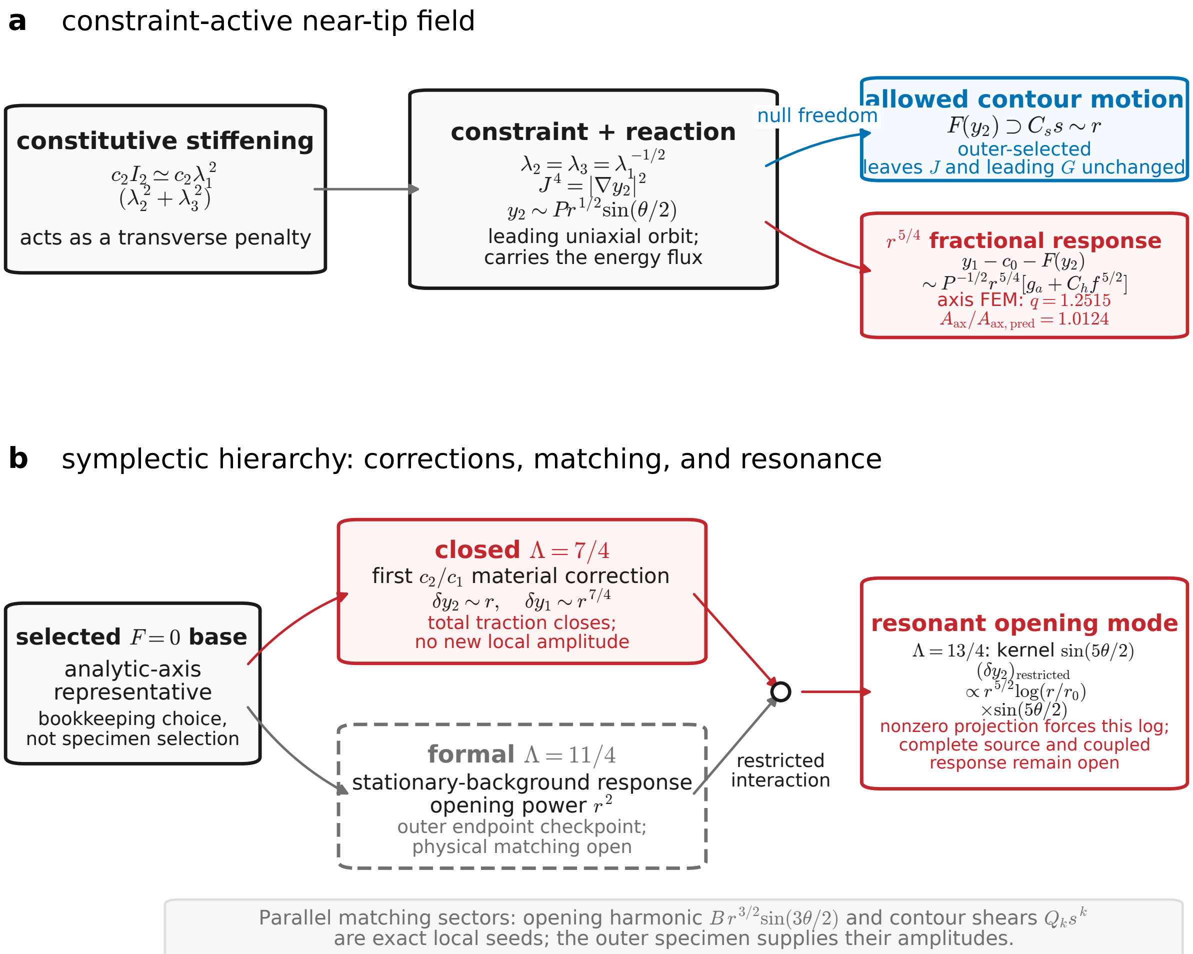

Figure 2: Constraint physics and the symplectic higher-order map. (a) Constitutive stiffening produces the constrained leading orbit, an outer-selected contour motion, and the $r^{5/4}$ fractional response tested in Fig. 7. (b) On the $F = 0$ bookkeeping representative, the $\Lambda = 7/4$ correction closes. Its restricted interaction with the formal $\Lambda = 11/4$ checkpoint reaches the $\Lambda = 13/4$ resonance and forces a formal logarithmic opening channel. The complete coupled response and matched logarithmic amplitude remain open.

The higher grades carry different physics. At $\Lambda = 7/4$, the I_2 term reappears as the first finite constitutive correction after imposing the leading constraint. At $\Lambda = 11/4$, the remaining base residual shows that the leading constrained orbit is not stationary at every later grade. In the audited restricted interaction, these routes meet the $\Lambda = 13/4$ opening kernel. Its nonzero projection requires a logarithmic companion in that formal coefficient.

Turning the pairing into a finite-radius extractor for B and Q_k would require the full reaction-carrying endpoint form and its adjoint modes. That is beyond the present normal-opening result. The amplitude used below is instead obtained directly from the normal face displacement, $y_2 \propto \sqrt{r}$. The leading field and its energy flux require neither the coupled extractor nor a completed all-order expansion.

6 Parameter-free relations and finite-element cross-checks

The locally uniaxial state gives several measurable predictions. Once the amplitude P is obtained from the crack-face opening, Eq. (23) gives predictions with no adjustable constants. A $c_2 = 0$ sheet shares the leading harmonic $r^{1/2}$ opening exponent and opening-row relation, but not the constrained transverse kinematics or the angle-independent compensated-Jacobian plateau. We test this constrained picture with finite elements that do not use it as input. A direct signature is the Jacobian plateau,

$$J\,r^{1/4} = \sqrt{P/2} \qquad \text{(independent of } \theta\text{)}, \tag{30}$$

and the full set is measured on the pure-shear strip of Fig. 1a:

relation	status (FEM)
$G = \lim \mathcal{J} = h\,W_\infty$ (35)	0.00–0.15% ($\lambda = 1.3$–2.2), unchanged over tested $a = 2$–5
P measured vs. $P(\lambda)$ of (35)	2.2–3.0%, entire load range (Fig. 3)
$J\,r^{1/4} = \sqrt{P/2}$, flat in θ	spread 3.2–9.1% (control 101.5–112.2%)
$Y_1 - c_0 \sim A_{\mathrm{ax}} r^{5/4}$ at $\theta = 0$	$q = 1.25153$, $A_{\mathrm{ax}}/A_{\mathrm{ax,pred}} = 1.01242$ (Fig. 7)

The first two rows connect specimen loading to the tip amplitude. The third tests the constrained Jacobian against the $W(I_1)$ control. All quantitative comparisons shown here use the Rivlin–Thomas strip, whose remote state gives $\mathcal{J}$ in closed form in Sec. 7. The near-tip field is not prescribed in the finite-element model. Figure 3 compares the measured opening amplitude with the prediction $P(\lambda)$, which has no adjustable constant. Crack lengths $a = 2$–5 collapse onto one curve, as expected from the steady pure-shear energy balance.

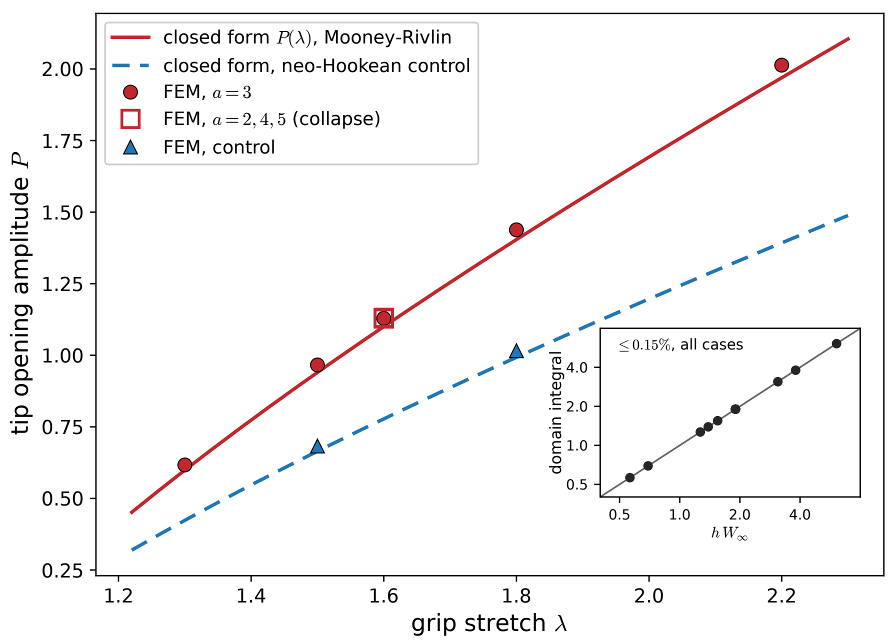

Figure 3: Measured near-tip amplitude P (markers) and the closed-form prediction $P(\lambda)$ from Eq. (35) (line). Results for crack lengths $a = 2$–5 at $\lambda = 1.6$ are shown by open symbols. The 2–3% offset is consistent with the finite fitting window and resolved core. The inset compares the domain integral $\mathcal{J}$ with hW_∞. The difference is at most 0.15% for all loads and crack lengths.

Figure 4 shows the computed state from the whole specimen down to the tip.

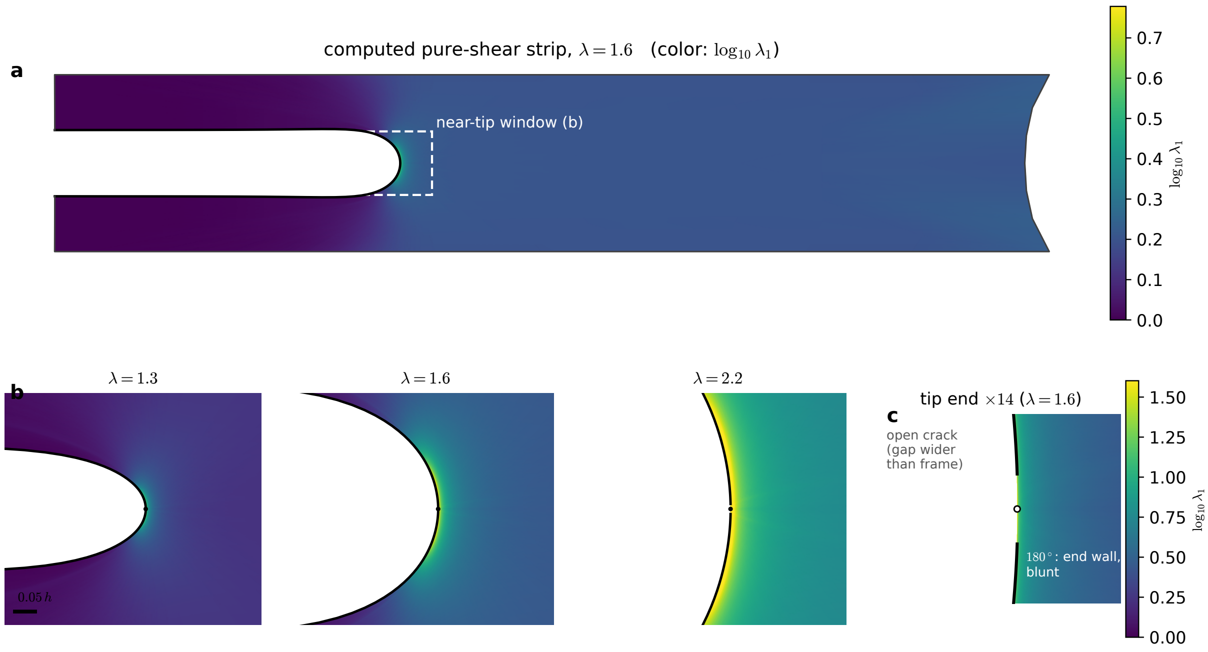

Figure 4: Finite-element solution for the pure-shear strip. Color denotes $\log_{10}\lambda_1$. (a) Full specimen at $\lambda = 1.6$. The upper half is reconstructed by Mode-I symmetry. (b) Near-tip fields at $\lambda = 1.3$, 1.6, and 2.2. The amplitude P is measured separately from each solution. (c) Tip field at $\lambda = 1.6$ with fourteen-fold greater magnification. The rounded cap is the traction-free core of the mesh, and the dot marks the tip material point. The resolved vertical tangent is compatible with Eq. (19), but does not separate its two crack-parallel terms.

The strip provides the specimen-scale comparison and Jacobian plateau. The quantitative plateau values distinguish the MR material from the $c_2 = 0$ control in Fig. 5. The field maps in Fig. 6 show the spatial region over which the normalized plateau is approached.

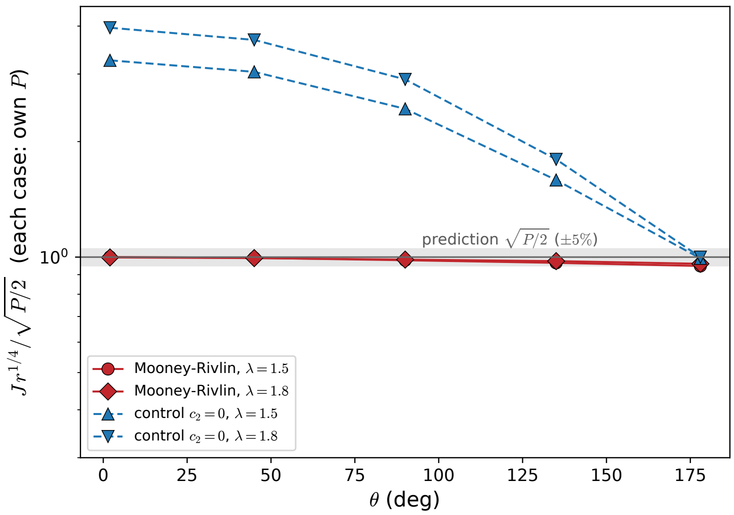

Figure 5: Window-averaged $Jr^{1/4}$, normalized by $\sqrt{P/2}$, at two loads. The Mooney–Rivlin result is nearly independent of θ, as predicted by Eq. (30). The $c_2 = 0$ control has an angular spread of 101.5–112.2% and differs from the predicted level by up to a factor of four near the ligament.

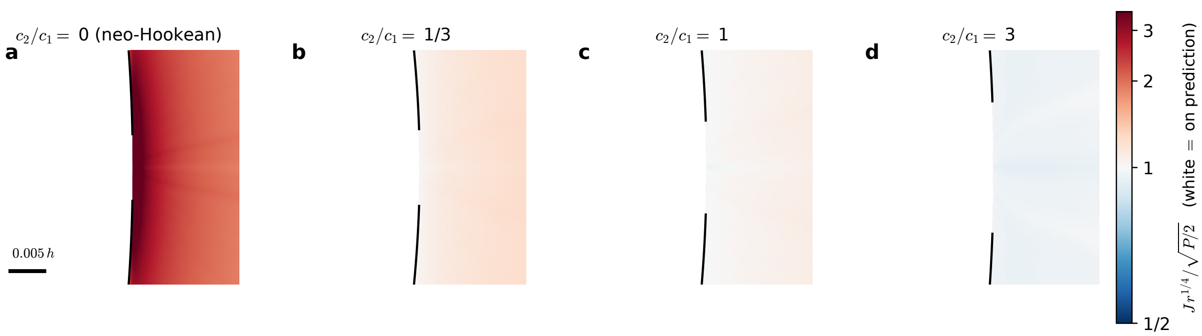

Figure 6: Normalized compensated Jacobian $Jr^{1/4}/\sqrt{P/2}$ at $\lambda = 1.6$. The window half-width is $0.015h$, and the scale bar is $0.005h$. The $c_2 = 0$ control in (a) is strongly angle dependent. The two-invariant cases $c_2/c_1 = 1/3$, 1, and 3 in (b)–(d) approach the predicted value, shown in white, throughout the near-tip region. All panels share the same scale, which is set by the strongly varying control. The low contrast in (b)–(d) reflects their closeness to the predicted plateau.

To test the dependence on material ratio, we repeat the strip calculation at $\lambda = 1.6$ for $c_2/c_1 = \frac{1}{3}, 1, 3$. Table 1 summarizes the common constrained-state signature.

Table 1: Material-ratio study at $\lambda = 1.6$. The middle three columns give relative errors or spreads in the energy, opening amplitude, and compensated-Jacobian plateau. The final column is the local log–log slope from a free finite-window fit of y_2. It diagnoses convergence toward the exact exponent $a_2 = 1/2$ and is not used to determine P.

c_2/c_1	G_J vs. hW_∞	P vs. $P(\lambda)$	plateau spread	finite-window opening slope
1/3	0.05%	2.6%	7.6%	0.478
1	0.03%	2.6%	5.1%	0.470
3	0.06%	2.6%	5.8%	0.453

Across the three ratios, the calculations recover the closed-form hW_∞ to better than 0.1%, the parameter-free amplitude prediction to 2.6%, and finite-window opening slopes close to 1/2, with the Jacobian plateau flat to a few percent. The $c_2/c_1 = 1/3$ case, whose constrained zone is shallowest ($r \lesssim 0.07\,h$), is marginally the least flat but still follows the prediction. The free opening-exponent fit decreases as c_2/c_1 grows even though the constrained zone becomes deeper. The fitted opening exponent is a finite-window diagnostic. The amplitude P is measured with the asymptotic 1/2 exponent fixed in the two-term fit, which has the same 2.6% error at all three ratios.

The normalization of the selected residual scales as $P^{-1/2}$. On either crack face, using $r = y_2^2/P^2$ at leading order and Mode-I symmetry,

$$y_1 - c_0 = \frac{C_s}{P^2} y_2^2 + \frac{g(\pi)}{P^3} |y_2|^{5/2} + \cdots . \tag{31}$$

Equation (31) motivates a direct numerical test. The normal displacement first determines P. The crack-parallel field may then be written

$$y_1 - c_0 = C_s s + r^q h(\theta) + \cdots .$$

On the intact axis, $\theta = 0$, both the regular $C_s s$ motion and the homogeneous $C_h s^{5/4}$ member vanish. This removes the two specimen-dependent coefficients and gives the fit

$$y_1(r, 0) = c_0 + A_{\mathrm{ax}} r^q + D r^{7/4}.$$

Figures 4 and 6 use the production strip sweep, and their $c_1 = c_2$, $\lambda = 1.6$ panels share the same stored solution. Figure 7 instead uses six new matching-circle configurations of the same strip boundary-value problem. Four cases at $R_m = 0.01h$ form the plotted core and angular sequence, while two additional cases test R_m. In each case the complete P2 strip trace drives a consistency solve on the exact inner cell restriction, from which the profile is sampled. The independently refined local submodel does not enter Fig. 7. Three overlapping exact-axis radial fit windows are applied to every profile while the core decreases from $10^{-5}h$ to $2.5\times10^{-6}h$ and the angular resolution doubles. The outermost-window result is $q = 1.25153$. The fitted axis amplitude is 1.24% above $A_{\mathrm{ax,pred}} = (4\sqrt{2}/5)P^{-1/2}$, with P obtained independently from the crack-face opening. Changing the matching radius from $0.005h$ to $0.02h$ changes the fitted exponent by at most 5.50×10^{-4}. A separate fit that leaves both q and the next physical power free returns $q = 1.24980$–1.25152 and $p_{\mathrm{next}} = 1.68971$–$1.74746$ over five windows. The 5/4 result is therefore not imposed by the $r^{7/4}$ nuisance term. This fitted p_{next} lies near the $r^{7/4}$ in-plane slot in the selected $F = 0$ ordering of Eq. (25). This is a consistency check on the radial ordering, not on that correction's angular profile or amplitude. Neither exponent is imposed in the fit. Here p_{next} denotes a physical power in y_1. The same rung has pencil label $\Lambda = 7/4$, while its opening component scales as r^1.

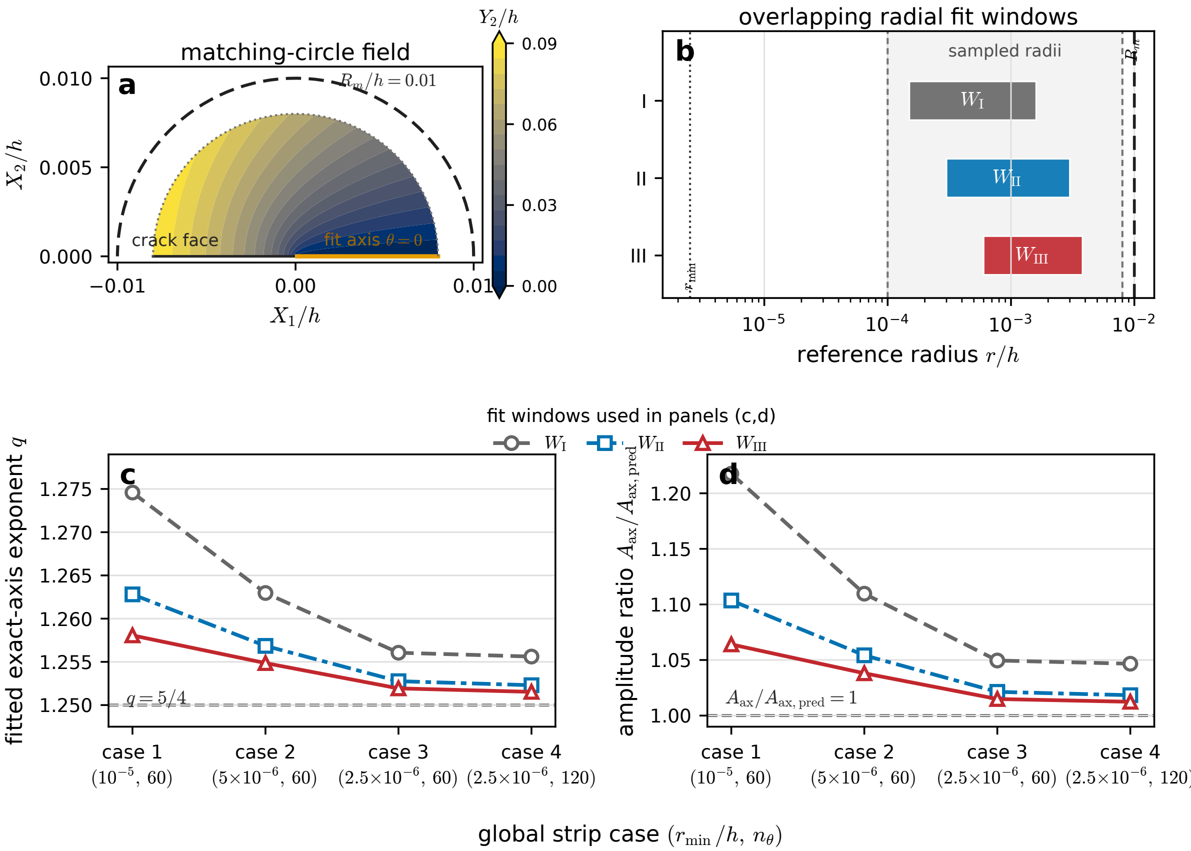

Figure 7: Matching-circle test of the $r^{5/4}$ in-plane residual for the $c_1 = c_2$, $\lambda = 1.6$ pure-shear strip. (a) Computed Y_2/h. The dashed semicircle is the internal matching interface, not a hole, and the orange segment is the sampled intact axis. (b) Windows I–III are overlapping fitting intervals on that same field. (c,d) Four global strip solutions successively reduce $r_{\min}$ and double the angular resolution. Fits to $y_1 = c_0 + A_{\mathrm{ax}} r^q + D r^{7/4}$ approach $q = 5/4$ and $A_{\mathrm{ax}}/A_{\mathrm{ax,pred}} = 1$, where $A_{\mathrm{ax,pred}} = (4\sqrt{2}/5)P^{-1/2}$ and P is measured independently. For the final outermost-window fit, $q = 1.25153$ and $A_{\mathrm{ax}}/A_{\mathrm{ax,pred}} = 1.01242$. Each x position is a simulation, whereas each curve is a fitting window. The expanded vertical scales are not error bars.

The full-angle field remains a harder decomposition because the regular and fractional powers are close over a finite annulus. In this separate full-angle channel, after the regular C_s-shaped background is removed, the finest field gives $q = 1.25349$ and agrees within 2.55% in relative L^2 with the permitted family $g_{\mathrm{a}}(\theta) + C_h \sin^{5/2}(\theta/2)$. This comparison supports the angular equation when its homogeneous member is retained. It does not select $C_h = 0$, and the fitted C_s and C_h remain window-sensitive specimen-level estimates.

Particle tracking provides an experimental route to the same separation. Qi et al. measured both the displacement map and deformation gradient around a plane-stress pure-shear crack, fitted the leading amplitude from the dominant gradient component, and mapped the radial range over which each component followed its asymptotic form [32]. Applied to a sheet with an independently calibrated positive I_2 coefficient, this protocol could measure the compensated-Jacobian plateau and fit P, C_s, and the detrended residual. Their Ecoflex study used a one-invariant generalized neo-Hookean model, so it supplies the measurement strategy rather than a test of the present constitutive prediction.

A focused half-disk calculation is retained as a distinct global boundary-value problem, not as quantitative validation of the strip field. Its imposed loading, high-load boundary folding, and the checks required before a cross-geometry comparison are documented in the ESI.

Numerical protocol. The Rivlin–Thomas strip supplies the quantitative G and $P(\lambda)$ tests, the Jacobian-plateau test, and the material-ratio study. Its energy release rate is known in closed form. Here pure shear names the remote strip loading, not a local crack-tip ansatz. The finite-element model solves the global nonlinear displacement boundary-value problem, without imposing the local analytical field. The calculations are performed with FEniCSx [33], solving the reduced sheet (2) on tip-focused rosette meshes with piecewise-quadratic displacements. In the strip, the fitted amplitude coefficient $\widehat{P}$ is measured on the stored 178° near-face proxy by the two-term fit $y_2 = \widehat{P}r^{1/2} + Cr$ of Sec. 4 in the window $r \in [3 \times 10^{-4}, 8 \times 10^{-3}]$. At leading order $\widehat{P} = P \sin 89°$. Throughout the numerical tables and figures it is reported under the label P as the estimator of the face amplitude, with the angular correction of less than 0.02% neglected. The representative $\lambda = 1.6$, $c_1 = c_2$ strip case passes the radial-mesh study reported in the ESI. For the residual test, an explicit internal semicircle supplies a matching trace and an exact inner-cell restriction for dense native-P2 sampling. A separate inner refinement uses the same complete P2 displacement trace. The reported exponent convergence comes from the matching-radius, core, and angular strip sequence rather than from imposing an asymptotic field on that circle. In the sampled $c_2 > 0$ strip full fields, the crack face remains out of tangential compression, so compressed-edge folding does not affect the Mooney–Rivlin comparisons. The meshes deliberately probe the mathematical $r \to 0$ limit of the reduced two-dimensional model. A laboratory sheet does not access that limit below t_s, where the field becomes three-dimensional. Comparison with experiment must instead use the overlap annulus in Eq. (24), when it is nonempty. These computations therefore test the reduced model over the stated finite-core windows, not the sub-thickness three-dimensional field. The complete protocol (specimen geometry and boundary conditions, mesh construction, solver settings, the definition of every estimator, the domain form of $\mathcal{J}$, and the convergence and window-sensitivity studies) is given in the ESI, together with the specimen schematic and the meshes.

7 Energy release rate

The energy release rate G is the energy the specimen supplies per unit of new crack area [34]. It reaches the tip as a flux of configurational (Eshelby) energy [35]. On a circle of radius r centered at the tip, let $\mathbf{N} = \mathbf{e}_r$ and let $t_i = P_{ij}N_j$ be the nominal traction from (3). The classical J-integral of Rice [36] is

$$\mathcal{J}(r) = \int_{-\pi}^{\pi} \big(W \cos\theta - t_i F_{i1}\big)\, r\, \mathrm{d}\theta. \tag{32}$$

We write $\mathcal{J}$ to distinguish the contour integral from the areal Jacobian $J = \det \mathbf{F}$. Using the total gradient F_{i1} rather than the displacement gradient does not change the integral because the net force $\oint t_i\, r\, \mathrm{d}\theta$ on the closed circle vanishes by equilibrium. Evaluating (32) on the leading field uses three leading-order facts. (i) The energy density obeys $W\, r \to c_1 P^2/4$, independent of θ. At leading order W is carried by the opening gradient alone. Its magnitude $|\nabla y_2| = \lambda_1$ is angle-free by (23). The c_2 and in-plane terms enter only at positive powers of r. (ii) The in-plane (row-1) flux vanishes in the tip limit. For the $F = 0$ bookkeeping representative this follows from the orders recorded in the ESI. Direct substitution of the physical truncated map including $C_s s$ gives the same limiting flux, although its finite-radius row-one orders differ. Thus no in-plane term contributes to

G. (iii) The opening (row-2) flux is finite: $t_2 \to c_1 P\, r^{-1/2} f$, so $t_2 F_{21}\, r \to c_1 P^2 f\left(\frac{1}{2}\cos\theta\, f - \sin\theta\, f'\right)$. Adding (i)–(iii), the θ-dependence cancels. The leading Eshelby flux density is the *constant* $c_1 P^2/4$ on every tip circle. Thus the limit $G = \lim_{r\to 0} \mathcal{J}(r)$ is

$$G = \frac{\pi}{2}\, c_1 P^2. \tag{33}$$

An exact symbolic limit for the superposed truncated map gives the same constant integrand, independent of g, g', C_s, and c_2. This shows directly that neither the regular $C_s s$ motion nor the $r^{5/4} g(\theta)$ residual contributes to the limiting flux. The energy release rate is carried by the leading opening field. Numerical quadrature of the full constitutive stress evaluated on this truncated map gives the same limit to 10^{-7} after extrapolation. The pure-shear finite-element results provide the separate specimen-scale cross-check of Sec. 6. For the $F = 0$ truncated representative the signed finite-radius error is an excess, $\mathcal{J}(r) - G = \pi c_2 P\, r^{1/2} + \cdots$, with fitted exponent 0.500. The opening-row c_2 traction flux, $-\int P_{2r}^{(c_2)} F_{21}\, r\, \mathrm{d}\theta = \pi c_2 P\, r^{1/2} + \cdots$, carries this correction. The component decomposition also shows that the angle-independent c_2 energy term integrates to zero against $\cos\theta$. This correction is caused by inserting the truncated local map into the full stress. It is not a failure of path independence for an exact equilibrium solution. Equation (33) plays for the constrained tip the role that Irwin's $G = K^2/E$ plays in linear theory [37]. It converts the field amplitude into the energy flux.

Only the leading opening term contributes to the limiting flux. A pair of field terms with physical radial exponents α_1, α_2 produces a flux $\sim r^{\alpha_1+\alpha_2-1}$ (we write α for a physical power, reserving Λ for the weighted pencil labels of Sec. 5). Thus the $r \to 0$ limit keeps only pairs with $\alpha_1 + \alpha_2 = 1$. Among the established regular outer exponents, the only such pair is the opening mode with itself ($\frac{1}{2} + \frac{1}{2}$). This is the finite-strain analogue of the quadratic self-contribution of the K-field, the universal linear-elastic tip field of amplitude K [25], to the linear fracture energy release rate. Any completed higher field with the positive exponents discussed in Sec. 5 is therefore invisible to the limiting $\mathcal{J}$. In the closed normal-opening sector, an opening harmonic at pencil location Λ pairs with the opening solution at $\Lambda' = \frac{3}{2} - \Lambda$ through (29). Extending this construction to candidate shears requires the still-open coupled operator and normalized extraction integrals. Three corollaries follow:

$$P = \sqrt{\frac{2G}{\pi c_1}}, \qquad P^{-1/2} = \left(\frac{\pi c_1}{2G}\right)^{1/4} \text{ (residual normalization)}, \qquad \sigma_{22}\, r = \frac{G}{\pi}. \tag{34}$$

At $c_2 \to 0$, Eq. (33) reduces directly to the plane-stress relation of Long, Krishnan and Hui: their Eq. (94) at hardening exponent $n = 1$ gives $\mathcal{J} = \mu\pi A^2/4$ [14], with μ their shear modulus, which is (33) with $c_1 = \mu/2$, and their amplitude *is* ours, since their Eq. (42a) reduces at $n = 1$ to $y_2 = A\, r^{1/2} \sin(\theta/2)$. Equation (33) therefore recovers the neo-Hookean result of Hui and co-workers as $c_2 \to 0$. The last relation in (34) also applies to sheets whose leading opening is $r^{1/2}\sin(\theta/2)$ because the leading Cauchy stress depends only on the opening equation. For hardening exponents $n \neq 1$ the opening exponent moves off $r^{1/2}$ and the relation takes the general form of their Eq. (94). This shared leading relation is an analytical corollary rather than a separate material discriminator.

Han and Li [22] extracted apparent indices N for the PK1 stress P_{22} and M for the Cauchy stress σ_{22} from finite-radius fits. With increasing applied strain, they found that M rises from approximately 1/2 toward 1, whereas N falls below 1/2 over a narrow small-strain interval before returning toward 1/2. The dip in N depends on c_2/c_1, while the limiting value of M is insensitive to this ratio. They related both trends to the expansion of the large-deformation zone around the tip. We interpret these apparent indices as the crossover from the outer small-strain field to the inner nonlinear field. This interpretation is consistent with Li and Moran's analysis of nested linear and nonlinear crack-tip regions in a neo-Hookean material [38]. The present analysis supplies the $r \to 0$ endpoint for the Mooney–Rivlin sheet. Along their fixed 45° ray, $P_{22} \sim r^{-1/2}$ and $\sigma_{22} \sim r^{-1}$. It also explains the material-ratio insensitivity of the limiting exponents, because the stress powers are neo-Hookean-like on the constraint manifold and the I_2 contribution is kinematic. Their single-ray, finite-window stress fits test the crossover and these limiting indices. They do not resolve the $r^{5/4}$ displacement residual, its angular profile, C_s, or C_h.

For the clamped pure-shear strip of reference height h [31], the remote boundary gives $\mathcal{J}$ without a numerical calculation. The far field ahead of the crack is the pure-shear state $(1, \lambda, 1/\lambda)$, for which $I_1 = I_2$, so

$$G = h\,(c_1 + c_2)\big(\lambda^2 + \lambda^{-2} - 2\big), \qquad P(\lambda) = \sqrt{\frac{2h\,(c_1 + c_2)\big(\lambda^2 + \lambda^{-2} - 2\big)}{\pi c_1}}. \tag{35}$$

The ratio c_2/c_1 enters Eq. (35) even though it cancels from (33): at equal applied stretch, a Mooney–Rivlin strip drives a larger P than a neo-Hookean strip of the same c_1. Section 6 compares this prediction with the measured tip amplitude from the finite-element model. The same opening-amplitude combination in (33) also appears in a different constitutive and kinematic setting. For compressible Ogden–Ball materials under finite *plane strain*, the closed-form energy flux of Le and Stumpf (their Eq. (6.23), with their amplitude A_1 and opening coefficient a) [23] reduces at power index $\alpha = 2$ to $(\pi/2)A_1 a^2$ with opening $a\,r^{1/2}\sin(\theta/2)$. This is the same Irwin-type relation, carried in both settings by the same opening row. The comparison concerns only this energy relation and does not extend the plane-stress constraint to plane strain.

8 Discussion

Connection to failure criteria from uniaxial data. If a material cutoff r_c lies inside the constrained plane-stress annulus, the near-tip state there is asymptotically uniaxial with θ-independent magnitudes (23). A critical-stretch criterion $\lambda_1(r_c) = \lambda_c$ of the kind used for elastomers and soft composites [39] then takes a simple form here. Each fiber at reference distance r_c from the tip (like all lengths in this paper, r_c is measured in the undeformed sheet) is in the state of a uniaxial test specimen to leading order. This holds in every direction θ, not only on the ligament. Thus λ_c can be connected directly to a tensile test within the assumptions of the constrained field. Combining $\lambda_1(r_c) = (P/2)\,r_c^{-1/2} = \lambda_c$ with (33) gives the critical energy release rate in closed form,

$$G_c = 2\pi\, c_1 \lambda_c^2\, r_c, \tag{36}$$

which contains two additional material inputs. The critical stretch λ_c can be obtained from a tensile test, while the effective cutoff r_c may be interpreted as a network length scale in the spirit of Lake and Thomas [40]. Two limits should be kept in mind. The plane-stress asymptotics hold only in the annulus of Sec. 4. Below the sheet thickness, the field is three-dimensional, and a network-scale r_c generally lies below that cutoff. At sufficiently large tip stretch, the Mooney–Rivlin energy must also be replaced by a finite-extensibility model. Equation (36) is therefore a formal extrapolation, as critical-stretch criteria usually are. Its advantage is that the extrapolated state is uniaxial. We present it as a practical consequence of the constrained state, not as a new failure criterion.

Local fields and specimen selection. The local solution determines the opening, the uniaxial stretch state, the Jacobian plateau, and the energy relation. It predicts the $r^{5/4}g(\theta)$ structure on the intact-axis outer branch after regular contour motion is removed. The pure-shear energy balance selects P, while the global boundary-value problem must select C_s, any homogeneous C_h contribution, and the higher regular amplitudes. This separation between local form and specimen-dependent amplitudes is familiar in crack-tip mechanics, as in the HRR fields [41, 42]. The expansion is in distance from a fully nonlinear leading state, not in loading amplitude. The derivation separates the determinant-null function $F(y_2)$ from the residual. It does not set the physical coefficient C_s to zero.

A matching-circle calculation resolves the residual without prescribing its asymptotic form. The complete quadratic displacement on a material circle is transferred from the strip, where it is already smooth enough to converge before the singular inner field. The local mesh can then be sampled or refined independently. This global–local strategy is established in linear fracture mechanics [43, 44]. Here the matching-radius, core, angular, amplitude, and free-power tests support the exact-axis 5/4 class. The full-angle field is consistent with the predicted ODE family, although the specimen-selected C_s and C_h have not reached a window-independent plateau. Full-field particle tracking provides an experimental route to the same separation. Outside the constrained annulus, the solution crosses over to the specimen-scale field, so finite-radius apparent indices can vary with radius and load [22].

9 Conclusion

We developed a radial symplectic framework for a constrained nonlinear crack tip and applied it to an incompressible plane-stress Mooney–Rivlin sheet. The I_2 term drives the local state toward uniaxial tension, giving the harmonic $r^{1/2}$ opening, angle-independent leading stretch magnitudes, the compensated-Jacobian plateau, and $G = (\pi/2)c_1P^2$. For a pure-shear strip this relation gives $P(\lambda)$ without a numerical specimen calculation, and the strip simulations support the amplitude and Jacobian predictions. Refinement toward the tip also recovers the exact-axis 5/4 residual exponent and its parameter-free amplitude to within 1.3%. The $c_2 \to 0$ limit recovers the plane-stress opening and energy relation of Long, Krishnan and Hui [14]. The two-invariant signature lies instead in the constrained transverse kinematics and Jacobian plateau.

The deformed-position trace and the r-weighted radial traction form the canonical pair, so the constraint reaction and the deformation evolve in one framework. The closed normal-opening sector gives the half-odd harmonic spectrum and a conserved symplectic pairing. On the selected $F = 0$, analytic-axis representative, the $\Lambda = 7/4$ material correction closes without an additional local amplitude. The separate $\Lambda = 11/4$ stationary-background calculation is retained as a formal endpoint checkpoint. Their audited restricted interaction reaches the $\Lambda = 13/4$ opening resonance. Its nonzero projection requires the formal coefficient to contain an $r^{5/2}\log(r/r_0)\sin(5\theta/2)$ companion. The complete same-grade source and coupled response remain open, and outer matching selects the net specimen amplitude. The physical in-plane field permits the regular contribution $C_s r\sin^2(\theta/2)$, whose amplitude is specimen-dependent. After this motion is separated, the constraint gives the $r^{5/4}$ angular ODE and its analytic-axis member $g(\theta)$. General matching may add the homogeneous term $P^{-1/2}C_h s^{5/4}$ at the same radial order. Numerical or experimental comparisons can therefore determine the matching coefficients. The present exact-axis comparison tests the predicted 5/4 structure without requiring either coefficient.

More broadly, the Mooney–Rivlin sheet shows how constitutive stiffening can reorganize crack-tip kinematics by becoming an effective constraint. Whether another soft-solid model develops the same structure must be decided from its own dominant balance. Finite-extensibility networks, and materials that stiffen selected invariants or directions, provide natural tests of this symplectic framework and its connection to measurable near-tip fields.

Conflicts of interest

There are no conflicts to declare.

Data availability

The analysis and simulation code and the finite-element data used in the figures are publicly available in version 1.2.0 of the public companion repository: https://github.com/tengzhang48/nonlinear-symplectic-mooney-rivlin-crack-tip/tree/v1.2.0.

Acknowledgements

The author acknowledges support from the U.S. National Science Foundation (NSF) under Grants CMMI-1847149 and CMMI-2517722. Computational resources were provided through the Advanced Cyberinfrastructure Coordination Ecosystem: Services & Support (ACCESS), including CloudBank, supported by NSF Awards No. 1925001 and No. 2505560, and Jetstream2, supported by NSF Grant No. 2005506.

Use of generative AI and AI-assisted technologies. Generative AI assistants—Claude (Anthropic), ChatGPT (OpenAI), DeepSeek, Kimi (Moonshot AI), and GLM (Zhipu AI)—were used for discussing the theory, developing and testing code, and revising language. The author reviewed, tested, and edited everything they produced and takes full responsibility for the content of the publication.

References

[1] J. P. Gong, Y. Katsuyama, T. Kurokawa, and Y. Osada. Double-network hydrogels with extremely high mechanical strength. *Adv. Mater.*, 15:1155–1158, 2003. doi: 10.1002/adma.200304907.

[2] J.-Y. Sun, X. Zhao, W. R. K. Illeperuma, O. Chaudhuri, K. H. Oh, D. J. Mooney, J. J. Vlassak, and Z. Suo. Highly stretchable and tough hydrogels. *Nature*, 489:133–136, 2012. doi: 10.1038/nature11409.

[3] X. Zhao. Multi-scale multi-mechanism design of tough hydrogels: building dissipation into stretchy networks. *Soft Matter*, 10:672–687, 2014. doi: 10.1039/C3SM52272E.

[4] C. Creton and M. Ciccotti. Fracture and adhesion of soft materials: a review. *Rep. Prog. Phys.*, 79:046601, 2016. doi: 10.1088/0034-4885/79/4/046601.

[5] R. Long, C.-Y. Hui, J. P. Gong, and E. Bouchbinder. The fracture of highly deformable soft materials: a tale of two length scales. *Annu. Rev. Condens. Matter Phys.*, 12:71–94, 2021. doi: 10.1146/annurev-conmatphys-042020-023937.

[6] F. S. Wong and R. T. Shield. Large plane deformations of thin elastic sheets of neo-Hookean material. *Z. Angew. Math. Phys.*, 20:176–199, 1969. doi: 10.1007/BF01595559.

[7] J. K. Knowles and E. Sternberg. An asymptotic finite-deformation analysis of the elastostatic field near the tip of a crack. *J. Elasticity*, 3:67–107, 1973. doi: 10.1007/BF00045816.

[8] J. K. Knowles and E. Sternberg. Finite-deformation analysis of the elastostatic field near the tip of a crack: reconsideration and higher-order results. *J. Elasticity*, 4:201–233, 1974. doi: 10.1007/BF00049265.

[9] J. K. Knowles. The finite anti-plane shear field near the tip of a crack for a class of incompressible elastic solids. *Int. J. Fract.*, 13:611–639, 1977. doi: 10.1007/BF00017296.

[10] R. A. Stephenson. The equilibrium field near the tip of a crack for finite plane strain of incompressible elastic materials. *J. Elasticity*, 12:65–99, 1982. doi: 10.1007/BF00043706.

[11] P. H. Geubelle and W. G. Knauss. Finite strains at the tip of a crack in a sheet of hyperelastic material: I. Homogeneous case. *J. Elasticity*, 35:61–98, 1994. doi: 10.1007/BF00115539.

[12] A. M. Tarantino. Thin hyperelastic sheets of compressible material: field equations, Airy stress function and an application in fracture mechanics. *J. Elasticity*, 44:37–59, 1996. doi: 10.1007/BF00042191.

[13] V. R. Krishnan, C.-Y. Hui, and R. Long. Finite strain crack tip fields in soft incompressible elastic solids. *Langmuir*, 24:14245–14253, 2008. doi: 10.1021/la802795e.

[14] R. Long, V. R. Krishnan, and C.-Y. Hui. Finite strain analysis of crack tip fields in incompressible hyperelastic solids loaded in plane stress. *J. Mech. Phys. Solids*, 59:672–695, 2011. doi: 10.1016/j.jmps.2010.12.005.

[15] R. Long and C.-Y. Hui. Crack tip fields in soft elastic solids subjected to large quasi-static deformation — a review. *Extreme Mech. Lett.*, 4:131–155, 2015. doi: 10.1016/j.eml.2015.06.002.

[16] Y. Liu and B. Moran. Large deformation near a crack tip in a fiber-reinforced neo-Hookean sheet. *J. Mech. Phys. Solids*, 143:104049, 2020. doi: 10.1016/j.jmps.2020.104049.

[17] Y. Liu and B. Moran. Crack tip fields in a neo-Hookean sheet reinforced by nonlinear fibers. *J. Mech. Phys. Solids*, 152:104406, 2021. doi: 10.1016/j.jmps.2021.104406.

[18] M. Mooney. A theory of large elastic deformation. *J. Appl. Phys.*, 11:582–592, 1940. doi: 10.1063/1.1712836.

[19] R. S. Rivlin. Large elastic deformations of isotropic materials IV. Further developments of the general theory. *Phil. Trans. R. Soc. Lond. A*, 241:379–397, 1948. doi: 10.1098/rsta.1948.0024.

[20] L. R. G. Treloar. *The Physics of Rubber Elasticity*. Clarendon Press, Oxford, 3rd edition, 1975.

[21] R. W. Ogden. Large deformation isotropic elasticity: on the correlation of theory and experiment for incompressible rubberlike solids. *Proc. R. Soc. Lond. A*, 326:565–584, 1972. doi: 10.1098/rspa.1972.0026.

[22] L. Han and L. X. Li. On the crack-tip stress singularity in the Mooney-Rivlin material. *Eng. Fract. Mech.*, 314:110734, 2025. doi: 10.1016/j.engfracmech.2024.110734.

[23] K. C. Le and H. Stumpf. The singular elastostatic field due to a crack in rubberlike materials. *J. Elasticity*, 32:183–222, 1993. doi: 10.1007/BF00131660.

[24] K. C. Le. On the singular elastostatic field induced by a crack in a Hadamard material. *Q. J. Mech. Appl. Math.*, 45:101–117, 1992. doi: 10.1093/qjmam/45.1.101.

[25] M. L. Williams. On the stress distribution at the base of a stationary crack. *J. Appl. Mech.*, 24:109–114, 1957. doi: 10.1115/1.4011454.

[26] B. Wang, Y. Wei, and H. Gao. From Muskhelishvili potentials to Williams crack-tip expansions. *J. Mech. Phys. Solids*, 214:106689, 2026. doi: 10.1016/j.jmps.2026.106689.

[27] A. Y. T. Leung, X. Xu, Z. Zhou, and Y. F. Wu. Analytic stress intensity factors for finite elastic disk using symplectic expansion. *Eng. Fract. Mech.*, 76:1866–1882, 2009. doi: 10.1016/j.engfracmech.2009.04.004.

[28] W. Yao, W. Zhong, and C. W. Lim. *Symplectic Elasticity.* World Scientific, Singapore, 2009. doi: 10.1142/6656.

[29] C. W. Lim and X. S. Xu. Symplectic elasticity: theory and applications. *Appl. Mech. Rev.*, 63:050802, 2010. doi: 10.1115/1.4003700.

[30] T. Zhang. Symplectic analysis for wrinkles: a case study of layered neo-Hookean structures. *J. Appl. Mech.*, 84:071002, 2017. doi: 10.1115/1.4036613.

[31] R. S. Rivlin and A. G. Thomas. Rupture of rubber. I. Characteristic energy for tearing. *J. Polym. Sci.*, 10:291–318, 1953. doi: 10.1002/pol.1953.120100303.

[32] Y. Qi, Z. Zou, J. Xiao, and R. Long. Mapping the nonlinear crack tip deformation field in soft elastomer with a particle tracking method. *J. Mech. Phys. Solids*, 125:326–346, 2019. doi: 10.1016/j.jmps.2018.12.018.

[33] I. A. Baratta, J. P. Dean, J. S. Dokken, M. Habera, J. S. Hale, C. N. Richardson, M. E. Rognes, M. W. Scroggs, N. Sime, and G. N. Wells. DOLFINx: the next generation FEniCS problem solving environment. Zenodo, 2023. doi: 10.5281/zenodo.10447666.

[34] A. A. Griffith. The phenomena of rupture and flow in solids. *Phil. Trans. R. Soc. Lond. A*, 221:163–198, 1921. doi: 10.1098/rsta.1921.0006.

[35] J. D. Eshelby. The elastic energy-momentum tensor. *J. Elasticity*, 5:321–335, 1975. doi: 10.1007/BF00126994.

[36] J. R. Rice. A path independent integral and the approximate analysis of strain concentration by notches and cracks. *J. Appl. Mech.*, 35:379–386, 1968. doi: 10.1115/1.3601206.

[37] G. R. Irwin. Analysis of stresses and strains near the end of a crack traversing a plate. *J. Appl. Mech.*, 24:361–364, 1957. doi: 10.1115/1.4011547.

[38] Y. Li and B. Moran. On small scale nonlinearity and nested crack tip fields in a neo-Hookean material. *Int. J. Fract.*, 249:62, 2025. doi: 10.1007/s10704-025-00880-0.

[39] C. Mo, J. R. Raney, and J. L. Bassani. Finite deformation near a crack tip terminated at an interface between two neo-Hookean sheets. *J. Mech. Phys. Solids*, 158:104653, 2022. doi: 10.1016/j.jmps.2021.104653.

[40] G. J. Lake and A. G. Thomas. The strength of highly elastic materials. *Proc. R. Soc. Lond. A*, 300:108–119, 1967. doi: 10.1098/rspa.1967.0160.

[41] J. R. Rice and G. F. Rosengren. Plane strain deformation near a crack tip in a power-law hardening material. *J. Mech. Phys. Solids*, 16:1–12, 1968. doi: 10.1016/0022-5096(68)90013-6.

[42] J. W. Hutchinson. Singular behaviour at the end of a tensile crack in a hardening material. *J. Mech. Phys. Solids*, 16:13–31, 1968. doi: 10.1016/0022-5096(68)90014-8.

[43] C. Song and J. P. Wolf. Semi-analytical representation of stress singularities as occurring in cracks in anisotropic multi-materials with the scaled boundary finite-element method. *Comput. Struct.*, 80:183–197, 2002. doi: 10.1016/S0045-7949(01)00167-5.

[44] E. T. Ooi and Z. J. Yang. A hybrid finite element-scaled boundary finite element method for crack propagation modelling. *Comput. Methods Appl. Mech. Eng.*, 199:1178–1192, 2010. doi: 10.1016/j.cma.2009.12.005.